



## Short Communication

## Hydrogen embrittlement of an interstitial equimolar high-entropy alloy

Hong Luo\*, Zhiming Li\*, Wenjun Lu, Dirk Ponge, Dierk Raabe

Max-Planck-Institut für Eisenforschung, Max-Planck-Straße 1, 40237, Düsseldorf, Germany



## ARTICLE INFO

## Keywords:

- A. Alloy
- B. Hydrogen permeation
- B. SEM
- C. Hydrogen embrittlement

## ABSTRACT

We investigated the hydrogen embrittlement mechanism in an interstitially carbon alloyed equimolar CoCrFeMnNi high-entropy alloy (HEA) through low strain rate tensile testing under in-situ hydrogen charging. The tensile ductility was significantly reduced by hydrogen charging. The failure mode of the interstitial HEA in presence of hydrogen was a combination of intergranular and transgranular fracture as well as microvoid coalescence. Aggregated nano-carbides act as potential sites for crack initiation. These findings show that the carbon alloyed equimolar high-entropy alloy is susceptible to hydrogen embrittlement.

## 1. Introduction

High-entropy alloys (HEAs) composed of multiple principal elements in equimolar or near-equimolar ratios with high mixing entropy have attracted significant attention in recent years [1–4]. This is mainly due to their simple crystal structure in concert with excellent mechanical properties particularly at cryogenic and ambient temperatures [5–8].

The five-element equimolar CoCrFeMnNi alloy is one of the most frequently investigated HEAs [9,10]. It is a single face-centered cubic (f.c.c.) solid solution with high thermodynamic stability and excellent malleability. The microstructure and mechanical properties of the equimolar CoCrFeMnNi HEA have been well-understood, including its twinning induced plasticity (TWIP) effect at room and cryogenic temperatures [10–13]. Recent work indicated that the equimolar CoCrFeMnNi HEA shows good resistance to hydrogen embrittlement [14]. It was observed that the material's strength and ductility can be even enhanced to some extent when tuning the hydrogen concentration [15]. These observations indicate that the CoCrFeMnNi HEA might be a promising structural candidate material for applications in hydrogen-propelled infrastructures and harsh, hydrogen-containing environments.

In spite of such progress, the mechanical properties of the fully recrystallized equimolar CoCrFeMnNi HEA at room temperature are still confined to a tensile strength regime below 600 MPa [5,16]. Recent studies show that interstitial alloying with carbon significantly improves the yield and ultimate tensile strength of both equimolar and non-equimolar transition metal HEAs while maintaining their good ductility [17,18]. This effect was attributed to the interstitial solid solution strengthening and the tunable precipitation strengthening

enabled by the presence of interstitial carbon. Despite their improved mechanical properties compared to interstitial free HEA, the hydrogen embrittlement resistance of the novel class of interstitial HEAs is still unknown. Motivated by this context, we investigate here the fracture behavior of the interstitial HEA  $\text{Co}_{19.9}\text{Cr}_{19.9}\text{Fe}_{19.9}\text{Mn}_{19.9}\text{Ni}_{19.9}\text{C}_{0.5}$  (at. %) upon in-situ hydrogen charging at room temperature. We present the hydrogen induced microstructural evolution upon tensile loading and discuss the mechanisms responsible for the hydrogen embrittlement behavior.

## 2. Material and methods

The interstitially alloyed equimolar CoCrFeMnNi HEA ingots were cast in a vacuum induction furnace with mixtures of the corresponding pure metals and carbon (purity > 99.8 wt. %) with predetermined composition of  $\text{Co}_{19.9}\text{Cr}_{19.9}\text{Fe}_{19.9}\text{Mn}_{19.9}\text{Ni}_{19.9}\text{C}_{0.5}$  (at. %). Samples with dimensions of  $10 \times 25 \times 60 \text{ mm}^3$  were machined from the original  $25 \times 60 \times 65 \text{ mm}^3$  as-cast blocks and subsequently hot-rolled in sequential passes at 900 °C to a total thickness reduction of 50%. The hot-rolled alloy sheets were homogenized at 1200 °C for 2 h in Ar atmosphere followed by water-quenching. The samples were cold-rolled to a total thickness reduction of 60% and annealed at 1000 °C for 5 min in Ar atmosphere followed by water-quenching. The bulk chemical composition of the homogenized interstitial HEA was measured by wet-chemical analysis, revealing a composition of 0.53 C, 19.71 Co, 19.76 Cr, 20.38 Fe, 19.73 Mn, and 19.89 Ni (at. %).

Flat dog-bone-shaped tensile specimens with gauge dimensions of  $3 \times 10 \times 1 \text{ mm}^3$  were machined from the annealed HEA sheets. Tensile testing under in-situ hydrogen charging was conducted at a low initial strain rate of  $10^{-4} \text{ s}^{-1}$  (constant cross head speed) at room temperature

\* Corresponding authors.

E-mail addresses: [h.luo@mpie.de](mailto:h.luo@mpie.de) (H. Luo), [zhiming.li@mpie.de](mailto:zhiming.li@mpie.de) (Z. Li).

by using an Instron tensile machine [19]. For comparison, tensile testing without hydrogen charging has also been performed. Hydrogen charging was conducted for 24 h before tensile testing and continued during the ongoing tests in 0.1M NaOH solution at a cathodic current density of  $100 \text{ mA cm}^{-2}$ . Thermal desorption spectroscopy (TDS) was used to measure the hydrogen concentration introduced into the samples during charging process. TDS experiments were conducted immediately after tensile testing, covering a TDS range from  $25^\circ\text{C}$  to  $800^\circ\text{C}$  at a constant heating rate of  $26^\circ\text{C min}^{-1}$ . The base pressure inside the chamber before analysis was lower than  $4 \times 10^{-9}$  mbar, and the total hydrogen concentration ( $H_{\text{Total}}$ ) was determined by measuring the cumulative hydrogen desorbed over the temperature range of  $25^\circ\text{C}$  to  $800^\circ\text{C}$ .

The cross sections of the tensile tested specimens along the tensile direction were cut for microstructural observations placing focus on the regions close to the surface in the most strongly H-affected zones. The samples were prepared by mechanical grinding and polishing with SiC paper. Final polishing was conducted with colloidal silica suspension to ensure a deformation-free surface. Microstructural observations were performed by electron backscatter diffraction (EBSD) using a Zeiss-Crossbeam XB 1540 FIB scanning electron microscope (SEM) with a Hikari camera and the TSL OIM data collection software, and electron channeling contrast imaging (ECCI) using a Zeiss Merlin SEM [20,21]. The nano-carbides in the interstitial HEA were observed and analyzed by using transmission electron microscopy (Philips CM20 TEM) operated at 200 kV.

### 3. Results and discussion

Fig. 1a shows the overview of the initial microstructure in the interstitial HEA prior to hydrogen charging. The microstructure of the interstitial HEA is in fully recrystallized state containing a number of annealing twins, an observation similar to the HEA without C alloying [22]. Three grains in the same sample were selected for further ECCI analysis and the typical results are shown in Fig. 1b–d, respectively. ECCI probing has matured as a very capable method to observe

dislocation substructures [20,23]. The dislocation density in the HEA was observed to be very low after annealing at  $1000^\circ\text{C}$  for 5 min. Also, nano-carbide particles with an average size of 50–100 nm are found to be randomly distributed in the interstitial HEA sample.

Fig. 2a shows a typical high angle annular dark field scanning TEM (HAADF-STEM) image of the nano-carbides and the f.c.c. matrix. The dark field TEM image (Fig. 2b) and the corresponding selected area diffraction pattern (Fig. 2c) as well as simulation pattern (Fig. 2d) reveal that the observed nano-particles are f.c.c. structured  $\text{M}_{23}\text{C}_6$  carbides, consistent to previous observations in an interstitial non-equimolar HEA [17].

Fig. 3a shows the engineering stress-strain curves of the interstitial HEA with and without hydrogen charging. The ultimate tensile strength of the interstitial HEA without hydrogen is approximately 730 MPa, which is higher than that of the carbon-free HEA. The elongation is approximately 58%, which is slightly lower compared to that of the carbon-free HEA [5]. A slight increase in yield strength was observed in the hydrogen charged HEA, which might be due to the solid solution strengthening effect of hydrogen. However, the elongation drops to approximately 46% when exposed to hydrogen. One has to note in that context that an enhancement of strength and ductility due to the presence of hydrogen, as observed in the carbon-free equimolar reference CoCrFeMnNi HEA [15], is not found in the present interstitial HEA. This is attributed to two effects. First, in interstitially alloyed HEAs carbides can act as potential sites for crack initiation. Second, the stacking fault energy of the carbon alloyed HEA studied here is higher than that of its carbon-free reference alloy, reducing the role of twinning on strain hardening. Both effects are discussed in more detail below.

The total hydrogen concentration  $H_{\text{Total}}$  in the hydrogen charged interstitial HEA was approximately 5.65 wt.ppm according to the hydrogen desorption rate curves shown in Fig. 3b. The total hydrogen content includes the hydrogen fractions stored in the lattice and that trapped in reversible and irreversible trapping sites.

Fig. 4a and b show the overview fracture morphologies of the interstitial CoCrFeMnNi HEA with and without hydrogen charging, respectively. The high magnification images for the edge and inner

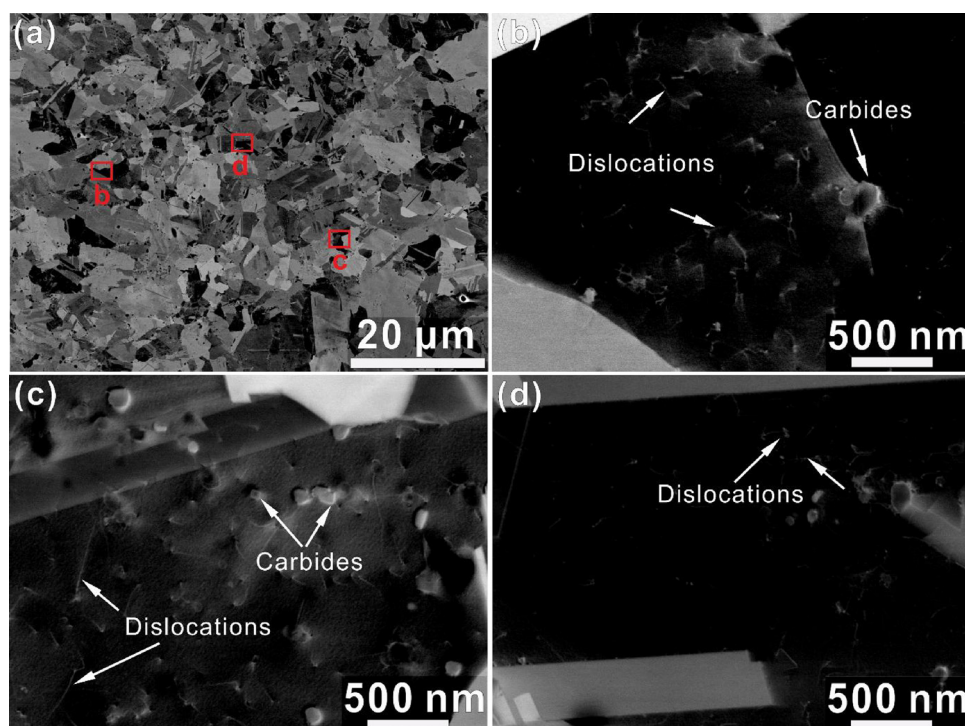
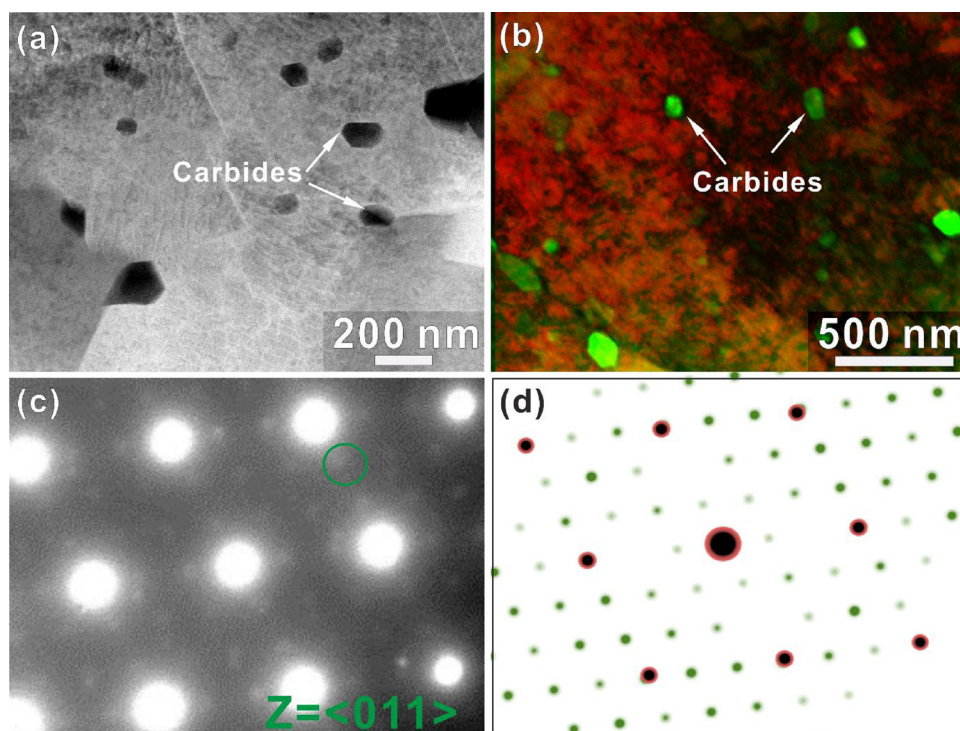
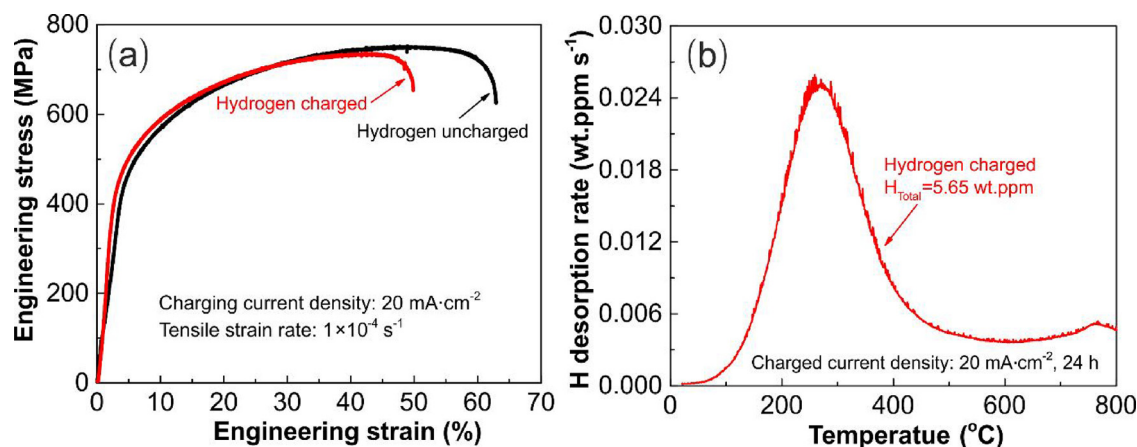


Fig. 1. Microstructure of the interstitial HEA after recrystallization annealing at  $1000^\circ\text{C}$  for 5 min: (a) ECC image with relatively low magnification; (b)–(d), ECC images of the selected grains in (a). ECC: Electron Channeling Contrast.



**Fig. 2.** TEM analysis of the nano-carbides in the interstitial HEA after recrystallization annealing: (a) High angle annular dark field (HAADF) image. (b) TEM dark field image. (c) Selected area diffraction pattern. (d) Simulation diffraction pattern, red-austenite, green- $M_{23}C_6$  carbides. Note that the TEM sample was prepared by a FIB technique and may hence contain some FIB-induced dislocations. FIB refers to focused ion-beam.



**Fig. 3.** (a) Typical engineering stress-strain curves of the interstitial HEA samples with and without hydrogen charging. The samples were charged in 0.1M NaOH solution at a current density of  $20 \text{ mA cm}^{-2}$ . Three samples for each condition were tested to confirm reproducibility. (b) Typical hydrogen desorption rate curve of the hydrogen charged and tensile-tested samples.

regions of the interstitial HEA sample without hydrogen charging are shown in Fig. 4a<sub>1</sub> and a<sub>2</sub>, respectively. The fracture surface of the material without hydrogen charging has a completely ductile appearance, containing many dimples in both the edge (Fig. 4a<sub>1</sub>) and inner (Fig. 4a<sub>2</sub>) regions. In contrast, three distinctly different fracture morphology regions were observed on the fracture surface of the interstitial HEA when exposed to hydrogen charging (Fig. 4b). The corresponding high magnification images pertaining to these three regions I, II, III are shown in Fig. 4b<sub>1</sub>–b<sub>3</sub>, respectively. The fracture surface of region I (edge region) shows a brittle intergranular fracture morphology, which has also been reported in the hydrogen charged carbon-free equimolar CoCrFeMnNi HEA [15,24]. The possible causes for the intergranular fracture is likely to be hydrogen enhanced localized slip [25] and decohesion-related weakening of the grain boundaries [26,27] at very high hydrogen concentrations. Accordingly, the adjacent transitional region II shows a mixed brittle-ductile failure mode. The inner region III of the fracture surface shows a typical ductile fracture mode, indicating

that less hydrogen reached the center during electrochemical charging.

Fig. 5 presents the high magnification SEM images of the fracture surface shown in Fig 4b<sub>1</sub>. The quasi-cleavage fracture morphology observed in the sample edge region I as indicated by the river-shaped deformation patterns suggests ductile fracture along dislocation slip planes [28]. Previous studies [5] have also reported that planar dislocation slip is the prevalent deformation mode in the CoCrFeMnNi HEA. Such quasi-cleavage fracture morphologies along dislocation slip lines have been explained in terms of the hydrogen enhanced localized plasticity (HELP) mechanism [29–31]. Therefore, the dissolved hydrogen in the interstitial CoCrFeMnNi HEA is assumed to enhance the mobility of the dislocations and reduce the barrier for dislocation interaction, thus causing slip localization on the primary slip planes and promoting cleavage fracture.

To further understand the fracture behavior of the interstitial HEA upon hydrogen charging, a combined ECCI and EBSD analysis was conducted to reveal the cracks close to the sample surface region



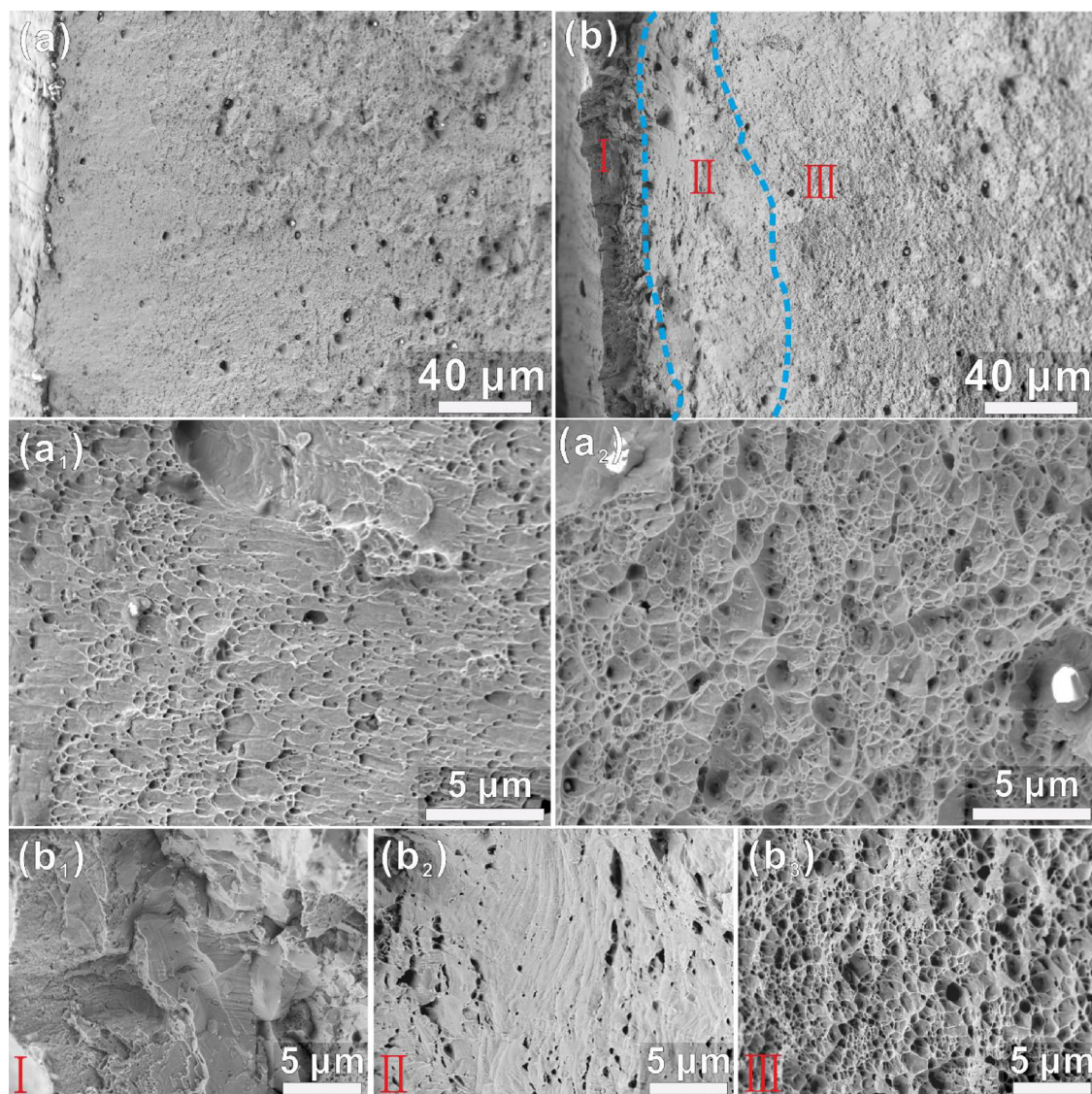


**Fig. 4.** Fracture surfaces of the tensile tested interstitial HEA with and without hydrogen charging. (a) Fracture surface of a reference sample without hydrogen charging. (b) Fracture surface of a sample exposed to hydrogen charging; the overview of the fracture surface shows brittle (I), transition (II), and ductile regions (III). (a<sub>1</sub>) and (a<sub>2</sub>) are high magnification SEM images of the edge and inner regions on the fracture surfaces of HEA sample without hydrogen charging. (b<sub>1</sub>), (b<sub>2</sub>), and (b<sub>3</sub>) are high magnification SEM images for the brittle (I), transition (II) and ductile regions (III), respectively, as marked in (b) for the interstitial HEA sample when exposed to hydrogen charging.

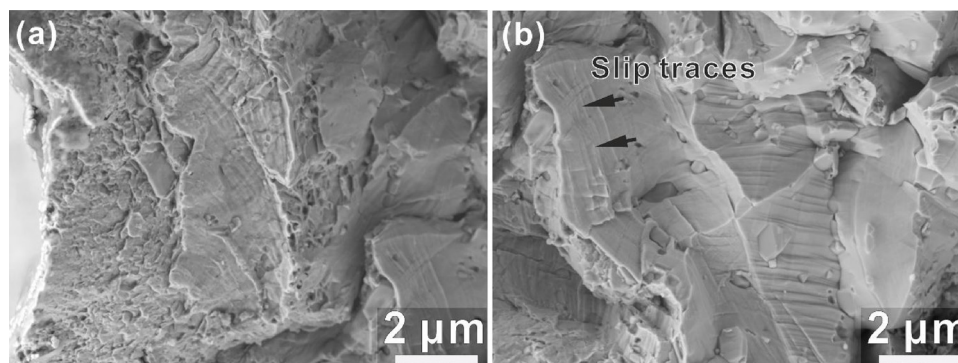


**Fig. 5.** High-magnification SEM images of the fracture surface at sample edge region I shown in Fig. 4b<sub>1</sub>. (a) Quasi-cleavage feature of the hydrogen charged and tensile tested interstitial HEA. (b) Intergranular feature indicates different slip traces on the fracture surface.



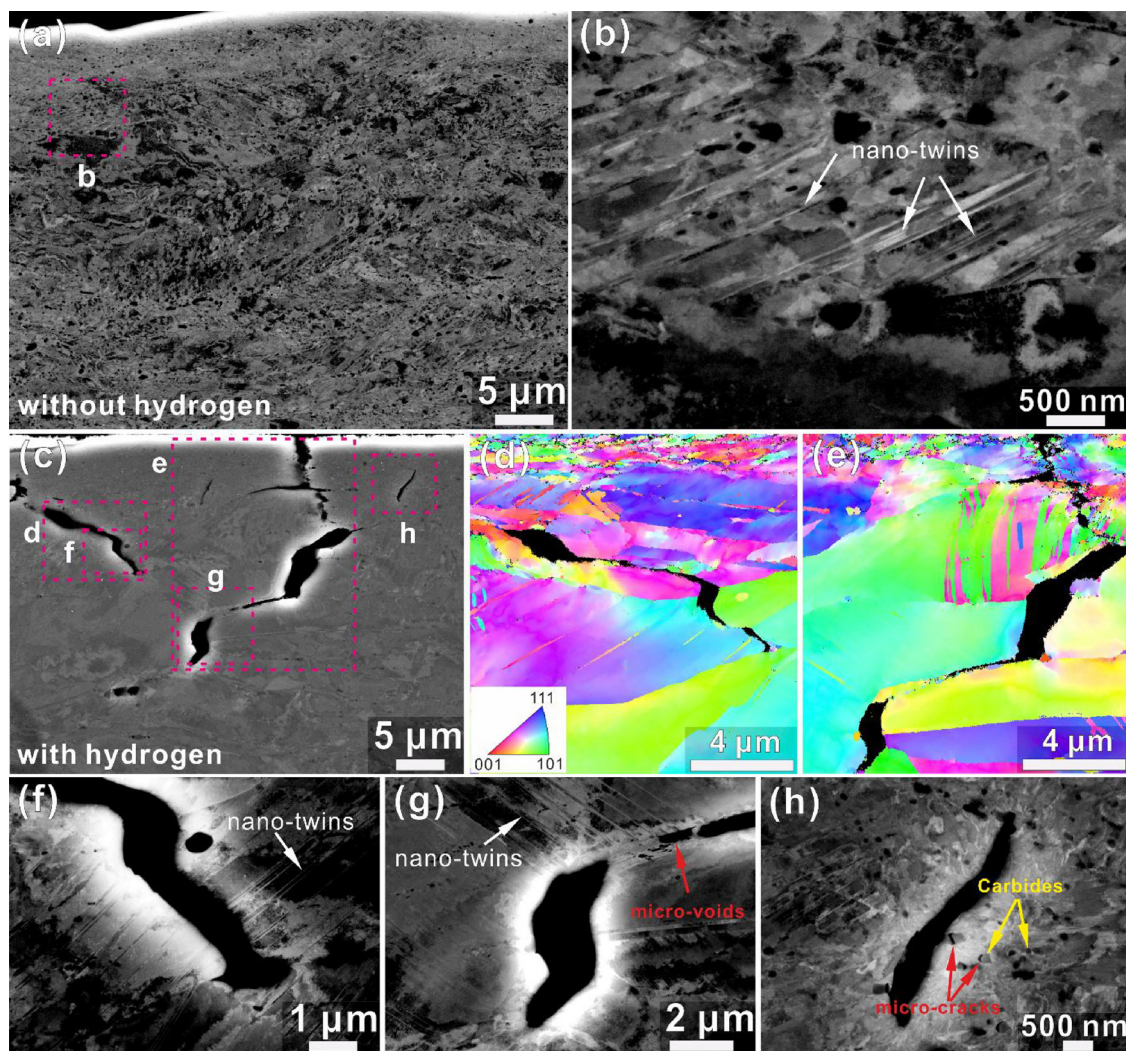


**Fig. 6.** Combined ECCI and EBSD analysis showing the microstructures close to the surface of the tensile tested interstitial HEA samples both, with and without hydrogen charging. (a), (b) ECC images of tensile tested samples without hydrogen charging. (c) Low magnification image of the tensile tested interstitial HEA with hydrogen charging. (d) and (e) are EBSD inverse pole figure (IPF) maps of the cracked regions marked in (c). (f)–(h) are ECC images showing the three different cracks marked in (c), respectively.

containing relatively high amounts of hydrogen. For comparison, the samples without hydrogen charging were also analyzed and the results are shown in Fig. 6. There are no any cracks in the interstitial HEA without hydrogen charging and a few deformation nanotwins were clearly observed as revealed in Fig. 6b. Compared to the carbon-free equimolar CoCrFeMnNi HEA, the interstitially carbon alloyed HEA did not show extensive twinning upon deformation. This is due to the fact that solute carbon increases the alloy's stacking fault energy (SFE) [32,33].

In the interstitial HEA exposed to hydrogen charging, cracks are found in regions I close to the sample surface, as show in Figs. 6c–h. Three main cracks, marked in Fig. 6c, were investigated in detail by using high-resolution EBSD (Fig. 6d and e) and ECCI (Fig. 6f–h). Both, intergranular and transgranular cracks can be observed from the inverse pole figure (IPF) maps in Fig. 6d and e. The initial interstitial HEA contains a large number of annealing twins prior to deformation (Fig. 1a). Under in-situ tensile loading, cracks can pass through these annealing twins as a type of transgranular fracture mode. Also, deformation induced nano-twins can be penetrated by these transgranular cracks (Fig. 6g).

It has been reported that the addition of carbon increases the SFE of the f.c.c. structured reference HEA [17]. Therefore, less twinning is observed in carbon alloyed interstitial CoCrFeMnNi HEAs when

subjected to tensile deformation. On the other hand, hydrogen has been reported to decrease the SFE in some f.c.c. structured alloys [34]. Further it was found that the twinning density increased during tensile deformation in a carbon-free equimolar CoCrFeMnNi HEA in the presence of hydrogen [15]. These results indicate that the enhancing effect of carbon on the SFE of the CoCrFeMnNi HEA is more dominant than the reducing effect of the hydrogen. It is likely that the resulting net effect of the two types of solutes on the SFE depends also on the actual hydrogen content that can be rendered into solution, a situation that is rather hard to control by conventional charging methods.

As in the current alloy the carbon effect seems to prevail, only few nano-twins were observed in the carbon-alloyed HEA during tensile deformation even in the presence of hydrogen compared to the case of the carbon-free reference HEA. This means that the beneficial effect of hydrogen promoted nano-twin formation, shown in a carbon-free HEA, is insignificant in the present interstitially carbon alloyed HEA.

In addition, crack propagation near submicron voids was also observed (Fig. 6g). Generally the micro-voids initiate at slip band intersections, and their growth and coalescence on the traces result in crack initiation and propagation [29]. Micro-void formation can be affected by several factors, such as strain distribution, dislocation reactions and local stress peaks [31,35]. Fig. 6h shows a crack initiating from aggregated nano-carbides, and some secondary micro-cracks connected to

nano-carbides can be observed near the main crack. As discussed above, the nano-carbides are randomly distributed in the f.c.c. matrix, i.e., some of them are located in the grain interior while others are in the grain boundary regions (Figs. 1 and 2). When nano-carbides aggregate at grain boundaries, hydrogen can be more easily accumulated and trapped at these grain boundary regions, causing intergranular fracture (Fig. 6g). Also, micro-voids can nucleate in the grain interior regions at the interfaces between the matrix and nano-carbides, leading to the transgranular failure (Fig. 6h) [36].

These features reveal that hydrogen embrittlement of the interstitially carbon alloyed HEA is caused by a combination of intergranular and transgranular fracture as well as by microvoid coalescence. These phenomena are strongly connected to the hydrogen enhanced localized plasticity mechanism which further promotes the slip concentration that is observed in this material. Also, it is noteworthy that the nano-carbides formed in the interstitial HEA are features that may potentially influence the hydrogen embrittlement behavior. However, the role of carbides on hydrogen embrittlement of traditional alloys is still under debate. For instance, Yokogawa et al. [37] concluded that the hydrogen embrittlement in 310S stainless steel is not related to the precipitation of carbides along grain boundaries while Thompson et al. [38] claimed that hydrogen embrittlement in sensitized 309S stainless steel is caused by the hydrogen accumulation at the interfaces of  $M_{23}C_6$  carbides precipitated along the grain boundaries. In the interstitial HEA studied here, we find more hints supporting the latter trend, namely, that the regions containing aggregated nano-carbides (Fig. 6h) are potential sites for crack initiation.

#### 4. Conclusions

Upon hydrogen pre-charging in 0.1M NaOH solution for 24 h at a current density of  $20 \text{ mA cm}^{-2}$  and subsequent in-situ tensile testing, the yield and ultimate tensile strength values of the interstitially equimolar CoCrFeMnNi HEA samples showed no significant reduction compared to those observed for samples without hydrogen. However, hydrogen caused the reduction in tensile elongation by approximately 12% through hydrogen assisted localized plasticity, crack formation and crack propagation. This means that the interstitially alloyed CoCrFeMnNi HEA is susceptible to hydrogen embrittlement and the failure mode in the presence of hydrogen is a combination of intergranular and transgranular fracture as well as microvoid coalescence. Aggregated nano-carbides were observed to act as potential sites for crack initiation.

#### Acknowledgments

This work was financially supported by the European Research

Council under the EU's 7th Framework Programme (FP7/2007–2013)/ERC Grant agreement 290998. The author (H.L.) is supported by the Alexander von Humboldt Stiftung.

#### References

- [1] J.W. Yeh, S.K. Chen, S.J. Lin, J.Y. Gan, T.S. Chin, T.T. Shun, C.H. Tsau, S.Y. Chang, *Adv. Eng. Mater.* 6 (2004) 299–303.
- [2] Y. Zhang, T.T. Zuo, Z. Tang, M.C. Gao, K.A. Dahmen, P.K. Liaw, Z.P. Lu, *Prog. Mater. Sci.* 61 (2014) 1–93.
- [3] D. Miracle, O. Senkov, *Acta Mater.* 122 (2017) 448–511.
- [4] Z. Li, K.G. Pradeep, Y. Deng, D. Raabe, C.C. Tasan, *Nature* 534 (2016) 227–230.
- [5] F. Otto, A. Dlouhý, C. Somsen, H. Bei, G. Eggeler, E.P. George, *Acta Mater.* 61 (2013) 5743–5755.
- [6] W.-R. Wang, W.-L. Wang, J.-W. Yeh, *J. Alloys Compd.* 589 (2014) 143–152.
- [7] Z. Li, C.C. Tasan, K.G. Pradeep, D. Raabe, *Acta Mater.* 131 (2017) 323–335.
- [8] Z. Li, D. Raabe, *JOM* 69 (2017) 2099–2106.
- [9] B. Cantor, I.T.H. Chang, P. Knight, A.J.B. Vincent, *Mater. Sci. Eng. A* 375–377 (2004) 213–218.
- [10] B. Gludovatz, A. Hohenwarter, D. Catoor, E.H. Chang, E.P. George, R.O. Ritchie, *Science* 345 (2014) 1153–1158.
- [11] G.D. Sathiaraj, P. Bhattacharjee, C.-W. Tsai, J.-W. Yeh, *Intermetallics* 69 (2016) 1–9.
- [12] G. Sathiaraj, P. Bhattacharjee, *J. Alloys Compd.* 647 (2015) 82–96.
- [13] D.-H. Lee, M.-Y. Seok, Y. Zhao, I.-C. Choi, J. He, Z. Lu, J.-Y. Suh, U. Ramamurty, M. Kawasaki, T.G. Langdon, *Acta Mater.* 109 (2016) 314–322.
- [14] Y. Zhao, D.-H. Lee, M.-Y. Seok, J.-A. Lee, M.P. Phaniraj, J.-Y. Suh, H.-Y. Ha, J.-Y. Kim, U. Ramamurty, J.-i. Jang, *Scripta Mater.* 135 (2017) 54–58.
- [15] H. Luo, Z. Li, D. Raabe, *Sci. Rep.* 7 (2017) 9892.
- [16] Z. Li, F. Körmann, B. Grabowski, J. Neugebauer, D. Raabe, *Acta Mater.* 136 (2017) 262–270.
- [17] Z. Li, C.C. Tasan, H. Springer, B. Gault, D. Raabe, *Sci. Rep.* 7 (2017) 40704.
- [18] Z. Wu, C. Parish, H. Bei, *J. Alloys Compd.* 647 (2015) 815–822.
- [19] M. Koyama, E. Akiyama, K. Tsuzaki, D. Raabe, *Acta Mater.* 61 (2013) 4607–4618.
- [20] I. Gutierrez-Urrutia, S. Zaefferer, D. Raabe, *Scripta Mater.* 61 (2009) 737–740.
- [21] I. Gutierrez-Urrutia, S. Zaefferer, D. Raabe, *JOM* 65 (2013) 1229–1236.
- [22] H. Luo, Z. Li, A.M. Mingers, D. Raabe, *Corros. Sci.* 134 (2018) 131–139.
- [23] J. Ahmed, A. Wilkinson, S. Roberts, *Philos. Mag. Lett.* 76 (1997) 237–246.
- [24] K. Nygren, K. Bertsch, S. Wang, H. Bei, A. Nagao, I. Robertson, *Curr. Opin. Solid State Mater. Sci.* 22 (2018) 1–7.
- [25] D. Ulmer, C. Altstetter, *Acta Metall. Mater.* 39 (1991) 1237–1248.
- [26] J. Kameda, C. McMahon, *Metall. Trans. A* 14 (1983) 903–911.
- [27] X. Wei, C. Dong, Z. Chen, K. Xiao, X. Li, *RSC Adv.* 6 (2016) 27282–27292.
- [28] R.C.P.S.C. Mittal, M.B. Deshmukh, *ISIJ Int.* 34 (1994) 211–216.
- [29] M.L. Martin, J.A. Fenske, G.S. Liu, P. Sofronis, I.M. Robertson, *Acta Mater.* 59 (2011) 1601–1606.
- [30] T. Neeraj, R. Srinivasan, J. Li, *Acta Mater.* 60 (2012) 5160–5171.
- [31] Z. Tarzimaghadam, D. Ponge, J. Klöwer, D. Raabe, *Acta Mater.* 128 (2017) 365–374.
- [32] A. Abbasi, A. Dick, T. Hickel, J. Neugebauer, *Acta Mater.* 59 (2011) 3041–3048.
- [33] R. Schramm, R. Reed, *Metall. Mater. Trans. A* 6 (1975) 1345–1351.
- [34] J. Hermida, A. Roviglione, *Scripta Mater.* 39 (1998) 1145–1149.
- [35] Z. Zhang, G. Obasi, R. Morana, M. Preuss, *Acta Mater.* 113 (2016) 272–283.
- [36] D. Symons, *Metall. Mater. Trans. A* 28 (1997) 655–663.
- [37] G. Han, J. He, S. Fukuyama, K. Yokogawa, *Acta Mater.* 46 (1998) 4559–4570.
- [38] A.W. Thompson, *Mater. Sci. Eng.* 14 (1974) 253–264.